City Research Online

City, University of London Institutional Repository

This is the accepted version of the paper.

This version of the publication may differ from the final published version.

1

Predicting the evaporation rate of stationary droplets with the VOF methodology for a wide range of ambient temperature conditions

4

5   George Strotos[1,a,*], Ilias Malgarinos[1,b], Nikos Nikolopoulos[1,c], ManolisGavaises[1,d]

6   [1]School of Engineering and Mathematical Sciences, City University London, Northampton
7   Square, EC1V 0HB, London, UK

8   [a] George.Strotos.1@city.ac.uk

9   [b] Ilias.Malgarinos.1@city.ac.uk

10   [c] Nikolaos.Nikolopoulos.1@city.ac.uk

11   [d] M.Gavaises@city.ac.uk

12   [*]Corresponding author

13

14   **Abstract**

15   This paper presents CFD predictions for the evaporation of nearly spherical suspended droplets
16   for ambient temperatures in the range 0.56 up to 1.62 of the critical fuel temperature, under
17   atmospheric pressures. The model solves the Navier-Stokes equations along with the energy
18   conservation equation and the species transport equations; the Volume of Fluid (VOF)
19   methodology has been utilized to capture the liquid-gas interface using an adaptive local grid
20   refinement technique aiming to minimize the computational cost and achieve high resolution at
21   the liquid-gas interface region. A local evaporation rate model independent of the interface
22   shape is further utilized by using the local vapor concentration gradient on the droplet-gas
23   interface and assuming saturation thermodynamic conditions. The model results are compared
24   against experimental data for suspended droplet evaporation at ambient air cross flow including
25   single- and multi-component droplets as well as experiments for non-convective conditions. It is
26   proved that the detailed evaporation process under atmospheric pressure conditions can be
27   accurately predicted for the wide range of ambient temperature conditions investigated.

28

29   **Keywords:** VOF, evaporation, multi-component, high temperature

30

1   INTRODUCTION

Droplet evaporation is an important phenomenon realized in several engineering and physical processes; it has been addressed in several textbooks, see selectively [1-4] and review articles [5-8]. Numerical modelling of droplet evaporation started with the idealized evaporation of a spherical, isolated, motionless and constant temperature droplet in an inert gas environment. Under these assumptions, Godsave [9] and Spalding [10] derived the widely known "d^2-law" which predicts that the squared diameter of the droplet reduces linearly with time. Following this approach, these strict assumptions were relaxed by taking into consideration the relative velocity between the air and the droplet, the transient droplet heating, the Stefan flow effects, the evaporation of multicomponent droplets and other secondary phenomena. The transient droplet heating was accounted with the Infinite Conductivity Model (ICM) [11] and the spatial temperature distribution inside the droplet with the Finite Conductivity Model (FCM) [12], the Effective Conductivity Model (ECM) [13] and the parabolic temperature profile model [14]. Regarding the Stefan flow effects which arise from the radial vapor motion, the models of Abramzon & Sirignano [13] and Yao et al. [15] are widely used, while there is a large variety of available heat/mass transfer correlations to account for the relative droplet-gas motion [7]. The performance of the aforementioned models was assessed in comparative studies such as in [16-19].

Modelling of multicomponent droplet evaporation has been also a challenging task since most of the fuels are mixtures of many hydrocarbon components. For a bi-component mixture, the preferential evaporation behavior obeys the distillation behavior of the two components, in which the most volatile species evaporates first followed by the vaporization of the less volatile component. The properties of the mixture depend, in addition to the local temperature, to the concentration. Thus, additional equations need to be solved, accounting for the variation of the species concentration in the liquid phase. Similar to the modelling of the thermal behavior of the droplet, the temporal evolution of the species concentration is simulated by using 0-D or 1-D models, usually known as the Infinite Diffusivity Models (IDM) [20-22] and the Finite Diffusivity Models (FDM) [23-26], respectively.

The aforementioned simplified approaches are suitable for Lagrangian spray models predicting the evolution of sprays plumes in combustion systems, comprised by a large number of polydispersed size droplets, as they do not require a lot of computational resources. On the other hand, their applicability is limited to spherical or near spherical droplets; moreover, they cannot give insight of the complex 3-D fluid and thermal transport processes taking place during

64   evaporation. Such models require solution of the Navier-Stokes equations along with the energy
65   and species transport equations both for the liquid and gaseous phases simultaneously. The
66   earliest CFD works on droplet evaporation were those of [27-29] who examined the evaporation
67   of single-component spherical droplets and derived useful correlations for the Nusselt and
68   Sherwood numbers, followed later by [30-34]. These works have revealed the importance of the
69   spatial distribution of the velocity, temperature and vapor concentration field and they can be
70   considered as benchmark cases for the validation of 0-D and 1-D models. Later, they were
71   extended to multicomponent fuels in [35-38] and to high pressure conditions in [39]. A common
72   feature of the aforementioned CFD works is that they use a grid fitted to the liquid-gas
73   interface; this provides an accurate representation of the flow field and allows for the
74   determination of the local momentum-heat-mass transfer rates, but they are limited to 2D
75   axisymmetric flows with no or low surface deformation as in [40]. On the other hand, the
76   Volume of Fluid (VOF) and Level Set (LS) methodologies among others can capture the 3D
77   droplet deformation (and even breakup), but with a less accurate prediction of the flow field at
78   the interface region. Recent works on droplet evaporation with the VOF methodology include
79   those of [41-44]. In these works a local evaporation model was used; Schlottke & Weigand [41]
80   used a virtual mass averaged velocity to calculate the source term of the continuity equation at
81   the interface region which improved the model performance. Furthermore, Strotos et al. [42]
82   and Banerjee [43] performed parametric studies for bi-component droplet evaporation while
83   Ghata & Shaw [44] studied the vaporization of fiber-supported droplets and included the effect
84   of thermocapillary stresses at the interface.

85   The present work examines the droplet evaporation using the solution of the Navier-Stokes
86   equations along with the energy conservation equation, the transport of species and the VOF
87   methodology for tracking the droplet interphase. The validation study examines single- and
88   multi-component droplets for a wide range of ambient temperature conditions under
89   atmospheric pressure. Relative to previous relevant CFD studies with the VOF methodology
90   resolving the complete fluid transport processes during vaporization, including the work of the
91   authors presented in [42], this is one of the first studies (at least to the authors' knowledge) that
92   examines droplet evaporation at temperature ambient conditions above the critical fuel
93   temperature and validates against experimental data the model for a wide range of temperatures.
94   The following sections include the description of the numerical model, the cases simulated,
95   followed by the model predictions for low and high ambient temperature conditions. The
96   conclusions of this work are summarized at the end.

97

2   MATHEMATICAL MODEL

2.1   Flow field equations

The numerical model involves the solution of the Navier-Stokes equations along with the solution of the transport equation of the liquid phase. The model is an extension of the one used in [45-47] including phase change. In addition, the numerical model employs the Volume of Fluid (VOF) methodology [48] for capturing the droplet liquid-gas interphase. In this methodology, the liquid phase is identified by the liquid volume fraction a_l (defined as the liquid volume in a cell divided by the cell volume) and its transport is given by:

$$\frac{1}{\rho_l}\left[\frac{\partial(a_l\rho_l)}{\partial t} + \nabla \cdot (a_l\rho_l\vec{u})\right] = -\sum_{k=1}^{Nsp} \dot{m}'''_{evap,k} \tag{1}$$

where ρ_l is the liquid phase density, $\vec{u}$ is the velocity vector and $\dot{m}'''_{evap,k}$ (kg/s/m^3) is the volumetric evaporation rate each of the *Nsp* species composing the liquid phase. The equation (1) can be used for an arbitrary number of phases *Nph* (here *Nph*=2), while the corresponding volume fraction of the gaseous phase can be obtained from the equality a_g=1-a_l. The momentum equations for both phases are written in the form:

$$\frac{\partial(\rho\vec{u})}{\partial t} + \nabla \cdot (\rho\vec{u}\vec{u}) = -\nabla p + \nabla \cdot [\mu(\nabla\vec{u} + \nabla\vec{u}^T)] + \rho\vec{g} + \vec{F}_{vol} \tag{2}$$

where $\vec{F}_{vol}$ is the volumetric force due to surface tension. This is calculated based on the Continuum Surface Force (CSF) approach of Brackbill et al. [49] and it is equal to:

$$\vec{F}_{vol} = \sigma\kappa\vec{n}\frac{\rho}{\frac{1}{2}(\rho_l+\rho_g)} \quad, \vec{n} = \nabla a \quad, \kappa = -\nabla \cdot \left(\frac{\vec{n}}{|\vec{n}|}\right) \tag{3}$$

where σ is the surface tension coefficient, $\vec{n}$ is the normal vector at the interface and κ is the curvature of the interface. Alternatively, the surface tension forces can be included in the momentum equations by using the Continuum Surface Stress (CSS) model by Lafaurie et al. [50] which inherently includes the effects of the variation of the surface tension coefficient along the interface. Equation (4) represents the CSS model, where **I** is the unit tensor and $\otimes$ is the tensor product of two vectors.

$$\vec{F}_{vol} = \nabla \cdot \left[\sigma\left(|\vec{n}|\mathbf{I} - \frac{\vec{n}\otimes\vec{n}}{|\vec{n}|}\right)\right] \quad, \vec{n} = \nabla a \tag{4}$$

Additionally, the transport equations for energy, vapor and liquid species concentration are solved:

126 $\quad \frac{\partial(\rho E)}{\partial t} + \nabla \cdot [\vec{u}(\rho E + p)] = \nabla \cdot \left[k\nabla T - \sum_{q=1}^{Nph}\left(a_q \sum_{k=1}^{Nsp} h_{q,k} \vec{J}_{q,k}\right) \right] - \sum_{k=1}^{Nsp} \dot{m}'''_{evap,k} L_k$ (5)

127 $\quad \frac{\partial(a_q \rho_q Y_{q,k})}{\partial t} + \nabla \cdot \left(a_q \rho_q Y_{q,k}\vec{u}\right) = \nabla \cdot \left(-a_q \vec{J}_{q,k}\right) + S_{Y,q}$ (6)

128 $\quad \vec{J}_{q,k} = -\rho_q D_{q,k,m} \nabla Y_{q,k}$, q=gas or liquid (7)

129   where $\vec{J}_{q,k}$ is the dilute approximation of the diffusion flux of species k at the mixture of phase

130   q (neglecting the Soret effect), $D_{q,k,m}$ is the diffusion coefficient of kth species in the mixture of

131   phase q (either gas or liquid). Equation (6) is solved in the gas phase (q=gas) for all the vapor

132   species (k=1÷Nsp) with a source term equal to $S_{Y,q} = \dot{m}'''_{evap,k}$. For the case of multicomponent

133   droplets, the same equation is also solved in the liquid phase (q=liquid) for all liquid species

134   with a source term equal to $S_{Y,q} = -\dot{m}'''_{evap,k}$, except of the main liquid species (k=Nsp), since

135   its concentration can be computed from the summation of the liquid species concentrations,

136   which must equal to one.

137   The properties of the pure components are assumed to be a function of temperature according to

138   [51, 52] and they are updated at every iteration during the numerical solution. The mixture

139   properties (either in the gas or the liquid phase for the case of multicomponent evaporation)

140   follow a mass average rule based on the concentration, while the gas phase density is obtained

141   by assuming incompressible ideal gas.

142   The numerical settings used for the simulations are: Laminar flow, explicit VOF solution with

143   the Geometric reconstruction scheme [53], Second Order Upwind (SOU) discretization [54] for

144   the momentum and energy equations, First Order Upwind (FOU) for the species transport

145   equations, Body Force Weighted (BFW) pressure interpolation scheme [55], pressure-velocity

146   coupling with the PISO algorithm [56], variable timestep with Courant number C=0.25 both for

147   the interface tracking and the whole computational domain (global Courant number).

148   The commercial CFD code ANSYS FLUENT v14.5 [55] has been utilized for the solution of

149   the flow equations with a number of user defined functions (UDF) for resolving the above

150   processes; more specifically, UDFs have been used for applying the automatic local grid

151   refinement technique and the interface sharpening algorithm [47] required to minimize the

152   interface diffusion which is promoted by the evaporation source terms. Moreover, the

153   evaporation rate model described in the next section is also implemented using UDF together

154   with the functions addressing the fluid, vapor and gas properties as function of local temperature

155   [51, 52].

156

2.2   Evaporation rate model

The evaporation rate is calculated as in [42, 43, 57, 58] by applying the simplified Fick's law at the liquid-gas interface cells:

$$\dot{m}''_{evap,k} = \rho_g D_{g,k,m} \left(\frac{dY_{g,k}}{dn} \right)_{surf} \qquad , \text{k=1}\div Nsp \tag{8}$$

The evaporation source term $\dot{m}'''_{evap,k}$ is obtained by multiplying equation (8) with $A_{l,cell}/V_{cell} = |\nabla a|$. The evaporation rate of equation (8) is independent of the interface shape and does not require any reference length or velocity. Although it is based on a diffusion law, the flow conditions are taken into account through the solution of the Navier-Stokes equations which advect the vapor and modify the local concentration gradient. Besides this simplified Fick's law, a more physically correct expression was also examined which takes into consideration the Stefan flow:

$$\dot{m}''_{evap,k} = \frac{\rho_g D_{g,k,m} \left(\frac{dY_{g,k}}{dn} \right)_{surf}}{1 - Y_{g,k,sat}} \tag{9}$$

Equation (9) has been used in Schlottke & Weigand [41] among others and it is valid only for single-component evaporation. For multi-component evaporation, the exact expression for the evaporation rate was given in Renksizbulut & Bussmann [38] but it was not examined here since it is more complicated and computationally expensive. For low evaporation rates and when the droplet temperature is not close to the boiling temperature (i.e. small Spalding numbers, B_M<<1), both expressions are valid.

The key parameter in the implementation of the evaporation rate model is the calculation of the concentration gradient magnitude $(dY_g/dn)_{surf}$. The interfacial cells are assumed to be saturated and the vapor saturation concentration Y_{sat} is calculated as a function of the cell temperature (and liquid composition when multicomponent evaporation is examined). An algorithm is used to identify the closest neighbor cell (subscript ∞) to the direction of the normal vector of the interface $\vec{n}$; this is illustrated in Fig. 1. Denoting as $\vec{d}$ the vector connecting the two cells, two options exist for the calculation of the concentration gradient (see details in Fig. 1) in non-orthogonal unstructured grids. The first one is the simplest but less accurate when the vectors $\vec{n}$ and $\vec{d}$ are not aligned. The second one is more accurate since it accounts for the angle between the two vectors; it works for all types of grid and it is the default method in the present model.

cell assumed saturated
$Y_{sat} = f(T_{cell})$
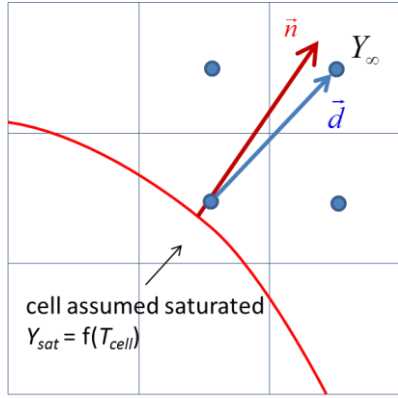
1. $\left(\dfrac{dY_g}{dn}\right)_{surf} = \dfrac{Y_{sat} - Y_\infty}{|\vec{d}|}$

2. $\left(\dfrac{dY_g}{dn}\right)_{surf} = \dfrac{Y_{sat} - Y_\infty}{|\vec{d}|} \dfrac{\vec{d}}{|\vec{d}|} \cdot \dfrac{\vec{n}}{|\vec{n}|}$

Fig. 1: Illustration of the two different methods employed for the estimation of the vapor concentration gradient at the liquid-gas interface. The 2nd method has been finally adopted in the present work.

Finally, the vapor diffusion coefficient $D_{g,k,m}$ of the kth species in the gas mixture, is obtained by using the dilute approximation (Eq. 10), in which $X_{g,k}$ is the mole fraction of species k in the gas phase and $D_{g,i,j}$ is the binary diffusion coefficient of species i in species j; the latter is a function of temperature:

$$D_{g,k,m} = \frac{1 - X_{g,k}}{\sum_{j,j \neq i}(X_{g,j}/D_{g,i,j})} \tag{10}$$

3   DESCRIPTION OF THE TEST CASES SIMULATED

The mathematical model used is validated against 3 sets of experimental data for suspended droplet evaporation for: (a) convective air flow conditions (experimental data of Daïf et al. [59]), (b) the data of Wong & Lin [60] and (c) under microgravity conditions in a quiescent gas environment (experimental data of Nomura et al. [61]). The cases examined are presented in Table 1; they all refer to atmospheric ambient pressure. As it can be seen, they cover a wide range of conditions including single- and multi-component evaporation, sub- and super-critical gas temperature conditions, low and moderate *Re* numbers, as also species with a large volatility difference (n-heptane and n-decane). More specifically, cases 1-3 correspond to the experimental data of Daïf et al. [59] who examined droplet evaporation at low temperature conditions and moderate *Re*

numbers for droplets consisting of n-heptane (case 1), n-decane (case 2) and a mixture of the two with 74% n-heptane (case 3). Case 4 corresponds to the experimental data of Wong & Lin [60] who examined the evaporation of n-decane droplets in a high temperature gas environment and low Re number flow. Cases 5-8 correspond to the experimental data of Nomura et al. [61], who investigated suspended n-heptane droplets in high temperature ambient conditions. Each set of the aforementioned experimental data is examined in a separate section in the present paper, in which the experimental and the numerical setup are presented in detail.

Table 1: Experimental conditions examined

| case	species	d_0	$T_{d,0}$	T_∞	u_∞	Re_0	ref
		[mm]	[K]	[K]	[m/s]		
1	C7	1.052	300	356	3.20	159	[59]
2	C10	1.386	315	348	3.10	210	[59]
3	C7-C10 74-26%	1.334	294	348	3.10	203	[59]
4	C10	1.961	315	1000	1.0	17	[60]
5	C7	0.700	300	471	~ 0	~ 0	[61]
6	C7	0.700	300	555	~ 0	~ 0	[61]
7	C7	0.700	300	648	~ 0	~ 0	[61]
8	C7	0.700	300	741	~ 0	~ 0	[61]

4   RESULTS & DISCUSSION

4.1   Evaporation at low temperature conditions. Experimental data of Daïf et al. [59]

In this section the numerical model is validated against the experimental data reported in Daïf et al. [59] for cases 1-3 of Table 1. These refer to subcritical ambient temperature conditions and include the evaporation of single- and multicomponent droplets at moderate *Re* numbers. In [59] the droplets were held in suspension at the spherical head of a capillary tube (400 and 200μm respectively), which was placed perpendicularly to the gas flow. They used a video camera to record the droplet diameter and an infrared thermo-graphic system to measure the droplet's surface temperature.

The computational domain, the boundary conditions and the grid used for these cases are shown in Fig. 2a; they are similar to these used in Strotos et al. [42]. The flow was assumed to be 2D-axisymmetric since the *Re* number is below 400 for all cases examined and the presence of the capillary tube is not expected to induce 3D effects. The spherical head of the suspender was assumed to be an adiabatic impermeable wall and the liquid contact angle was set to 10 degrees as in [42]. Regarding the initial conditions, uniform velocity, temperature and concentration fields were assumed. The grid used is unstructured with 2 levels of adaptive local refinement; this is based on the work of Theodorakakos & Bergeles [62] and implemented here as in Malgarinos et al. [45]. A grid independent solution is achieved by using 2 levels of local grid refinement as shown in Fig. 2b for the prediction of the dimensionless droplet volume temporal evolution. This is a good compromise between accuracy and computational cost which is approximately 1.7CPU-days for each second of physical time for the single-component cases and 2.3CPU-days/sec for the bi-component evaporation case.
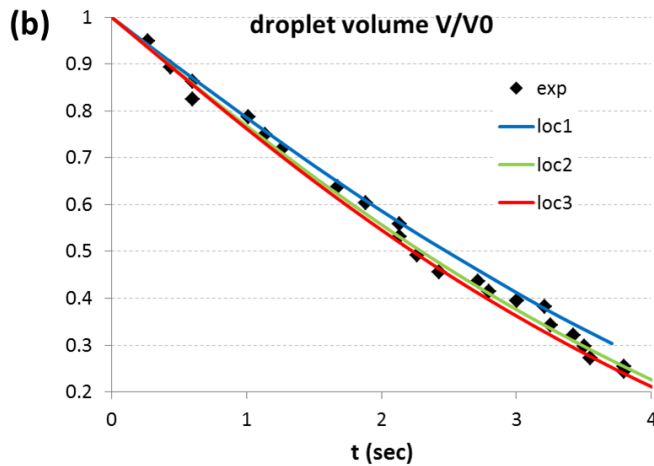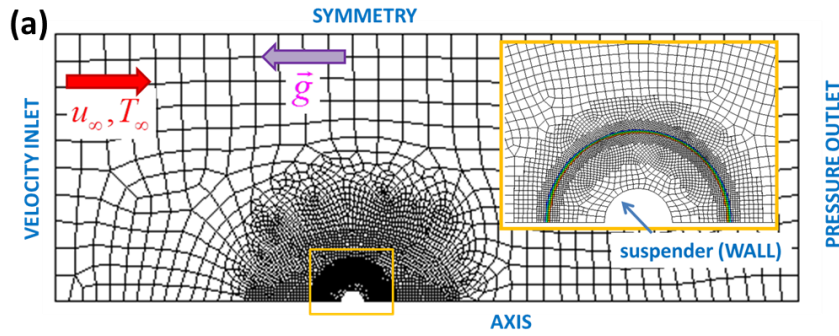
Fig. 2: (a) Computational domain and boundary conditions employed. The inset figure shows the grid topology around the liquid-gas interface for two levels of adaptive local grid refinement. (b) Temporal evolution of droplet's non-dimensional volume for the case 1 using one-, two- and three-levels of local grid refinement.

The temporal evolution of the non-dimensional droplet squared diameter and the mean droplet temperature for the cases of Daïf et al. [59] are presented in Fig. 3a and Fig. 3b, respectively. The predictions are in good agreement with the experimental data regarding the droplet size, while the wet-bulb temperature of n-decane is overestimated by 4°C; this is within the accuracy of previously published studies for the same case [25, 42, 63, 64]. Single-component droplets (cases 1 and 2) after an initial heat-up period follow the d^2-law and they reach the wet-bulb temperature corresponding to the experimental conditions. The two-component droplet (case 3) exhibits preferential evaporation in which the more volatile n-heptane evaporates first and then the less volatile n-decane follows. The relevant physical processes during the multicomponent evaporation have been discussed in depth discussed in Strotos et al. [42, 65].

259
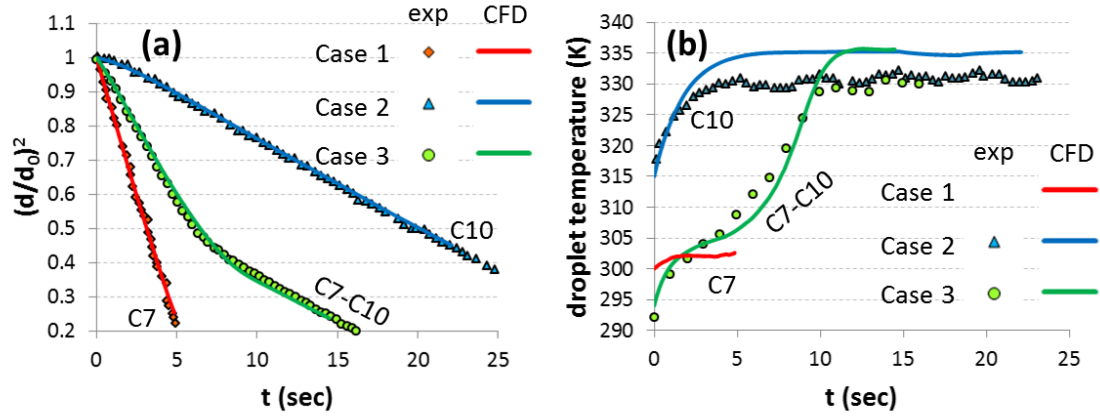
Fig. 3: Model predictions for the experimental data of Daïf et al. [59]. Temporal evolution of (a) droplet size and (b) mean droplet temperature. No experimental data were provided for the droplet temperature in case 1.

Initially, the spherical suspender lies at the centre of the droplet; under the action of gravitational and aerodynamic forces the droplet moves either upwards or downwards as shown in Fig. 4. The n-heptane droplet (case 1) is relatively light and moves upwards (opposite to the direction of gravity in Fig. 4), while the droplets of the other two cases are heavier and they move initially downwards (in the direction of gravity in Fig. 4). As the droplet evaporates and becomes lighter, the gravitational force become smaller compared to the aerodynamic one and the droplet progressively moves to the other side of the suspender. After reaching an equilibrium position, the droplets are held in touch with the suspender due to the adhesion forces. Behind the droplet, a large recirculation zone appears and its length is plotted versus the gas phase Re number in Fig. 5; the experimental data of Taneda [66] for a solid sphere are also shown. The wake length increases with increasing Re number and it is slightly restricted compared to the one formed under the same flow conditions behind a solid sphere. This is attributed to the liquid phase recirculation which moves the flow separation point towards the rear of the droplet and suppresses the length of the wake, as also reported previously in Sirignano [2].

279
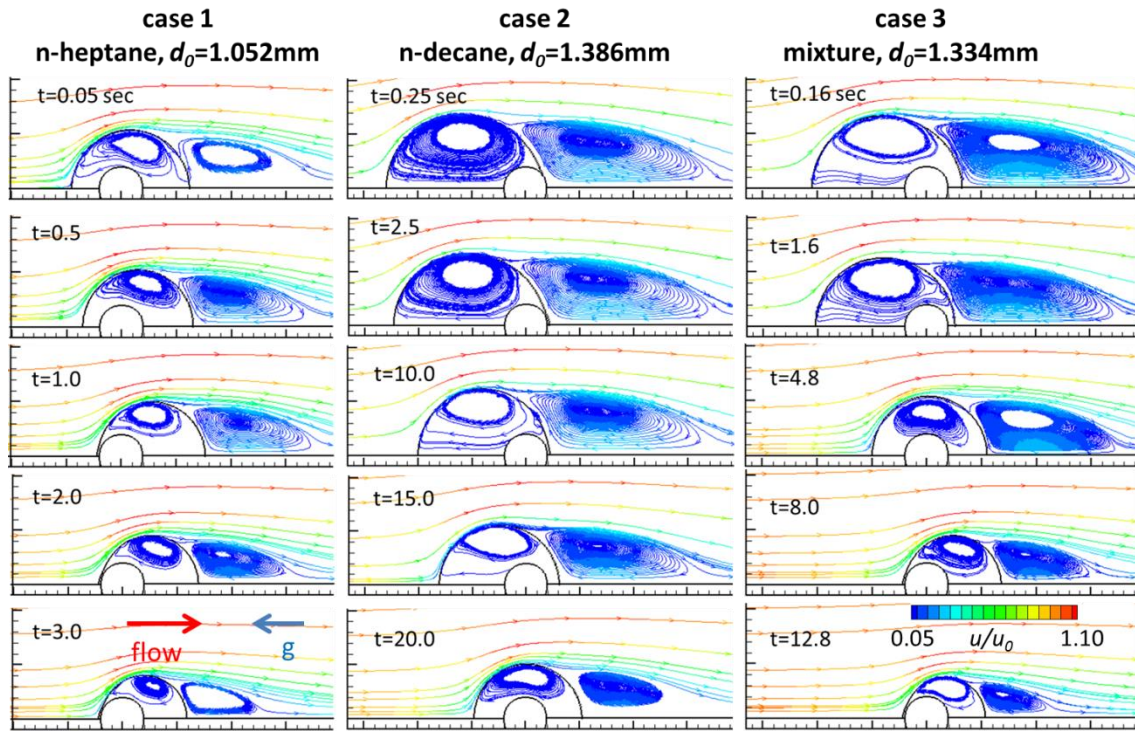
Fig. 4: Predicted transient droplet motion and flow field streamlines for the experiments of Daïf et al. [59] (cases 1-3).
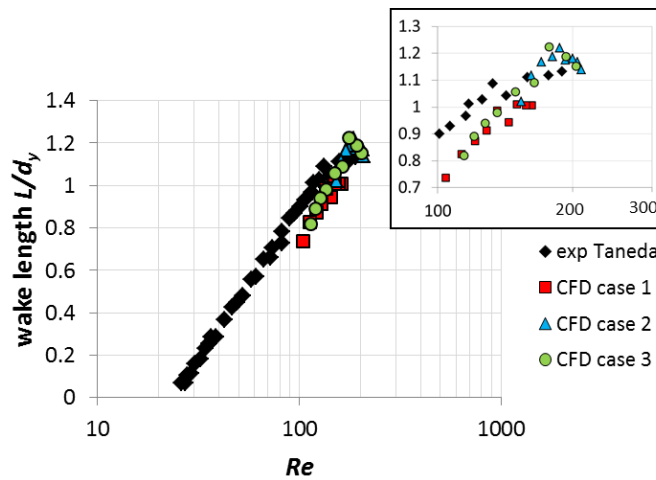
Fig. 5: Dependence of the wake recirculation length with the *Re* number for cases 1-3.

In Fig. 6 representative velocity, temperature and vapor fields are presented for the n-decane case at 0.25 and 20.0sec; the velocity field is depicted by the streamlines colored with the velocity magnitude. The spatial distribution of the temperature and the vapor field is influenced by the recirculation zones formed inside and behind the droplet, as also the presence of the solid suspender. Inside the droplet, a relatively cooler region is identified at the vortex core (as also

292   observed in [29, 30]), while at the wake behind the droplet the temperature and the vapor
293   concentration fields are similar between them and they are influenced by the gas phase vortex.

294
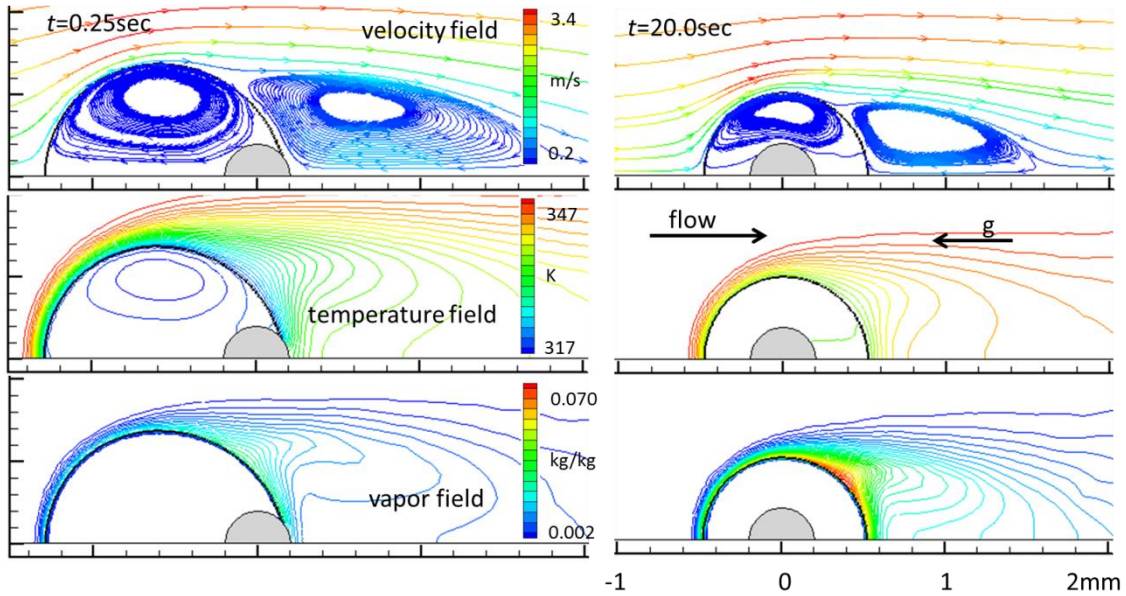
295

296   Fig. 6: Velocity streamlines, temperature and vapor concentration field for the n-decane droplet
297   (case 2).
298

299   In Fig. 7 the spatial distribution of the evaporation source term (in kg/m^{3}s) at selected time
300   instances is presented for the n-decane droplet; the non-interpolated contours shown correspond
301   to the region between VOF values equal to 0.01 and 0.99. As it can be seen, there is a narrow
302   region at the interface (2-3 cells) in which the evaporation source term is distributed and it
303   maximizes near the 0.5 iso-VOF line, in which the quantity $|\nabla a|$ maximizes too (see also the
304   inset figure at t=20sec). The thickness of this region in length units depends on the grid density,
305   but it has a minor effect on the overall evaporation process, as shown in Fig. 2b. The
306   evaporation rate increases with time, since the droplet temperature also increases; it is
307   interesting to observe that the maximum evaporation rate is observed around 30-40° away from
308   the front stagnation point, which was also observed in Shih & Megaridis [31]. The minimum
309   evaporation rate is observed near the point of flow separation at approximately 130-140°; this
310   behavior was also observed in Haywood et al. [28]. The spatial distribution of the evaporation
311   rate is not smooth and this is ought to the imperfect distribution of the VOF values over the
312   computational cells.

313
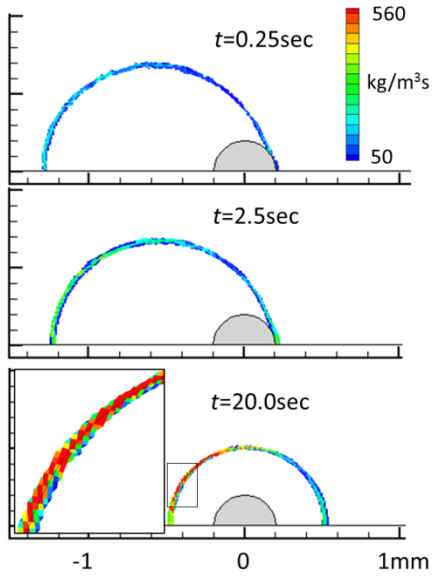
Fig. 7: Spatial distribution of the evaporation rate at different time instances for the n-decane droplet (case 2).

One of the parameters examined was the effect of the thermo-capillary flow (Marangoni effect) induced by the variation of the surface tension coefficient along the interface. This is achieved by using the CSS formulation [50] instead of the CSF model [49] in order to calculate the surface tension forces in the momentum equations. As it was also shown in Strotos et al. [42], the temperature along the interface does not exhibit large variations and the Marangoni effect does not affect the droplet evaporation for these specific cases. On the other hand, it seems to create a kind of unsteadiness by increasing the fluctuations of the droplet shape but without a noticeable effect on the liquid phase internal circulation; unsteadiness in thermo-capillary flows were also observed in Shih & Megaridis [32]. The single-component cases 1-2 were also examined by using the evaporation rate of equation (9). The results have shown that it has a negligible effect on the prediction of the phenomenon due to the low evaporation rate and thus it is not presented.

4.2 Evaporation at high temperature conditions. Experimental data of Wong & Lin [60]

The 4th case of Table 1 corresponds to the experimental data of Wong & Lin [60] who examined the evaporation of n-decane droplets in a supercritical gas environment (T_∞= 1000K, $T_{cr,C7}$=617.7K). The droplet was suspended at a ceramic shell attached to a 100μm glass filament; the droplet internal temperature distribution was measured by using thermocouples (25μm wire diameter and ~70μm bead diameter) placed at different positions inside the droplet.

338   This set of experimental data has been widely used in validation studies for 0-D and 1-D models

339   [16, 19, 63, 67, 68] as also in CFD studies by [30, 33], which assumed a spherical droplet shape

340   and neglected the presence of the shell-like suspender. In the present study the presence of the

341   suspender has been considered but assumed to be spherical since its exact geometry and

342   dimensions were not reported in the relevant paper.

343   The model predictions for the droplet size and the mean droplet temperature are shown in Fig. 8

344   by using the two variations of the evaporation model described in section 2.2, i.e using equation

345   (8) and (9), respectively. The predictions for the droplet size are satisfactory for both models

346   with the second one having a slightly higher evaporation rate at the beginning and lower at

347   subsequent times. In both cases the droplet's size regression deviates significantly from the d^2-

348   law due to the intense and long droplet heat-up period. During this period, the thermal

349   expansion of the droplet is more intense compared to the droplet evaporation and the droplet

350   size slightly increases; this phenomenon has been observed in [39, 69] among others. Regarding

351   the model predictions for the droplet temperature, the available experimental data for the droplet

352   temperature were obtained by placing three thermocouples at fixed positions (r/R_0=0, ±0.6).

353   Such information was difficult to be obtained with the current numerical setup since the droplet

354   moves over the suspender and also deforms. So, in Fig. 8 the model prediction for the mean

355   droplet temperature is presented, which is closely related to the measured quantities. The

356   temperature prediction is in accordance with the experimental measurements but this time the

357   simplified Fick's model of eq (8) has a better performance predicting accurately the wet-bulb

358   temperature. The present results are within the accuracy of the results obtained with other

359   numerical methodologies mentioned at the beginning of this section. It has to be noted that at

360   the latter stages of evaporation, the interface diffusion problems associated with the VOF

361   methodology become more pronounced and are more intense for high evaporation rates; this

362   explains why the droplet temperature predicted with equation (9) further increases for t>2.5sec.

363
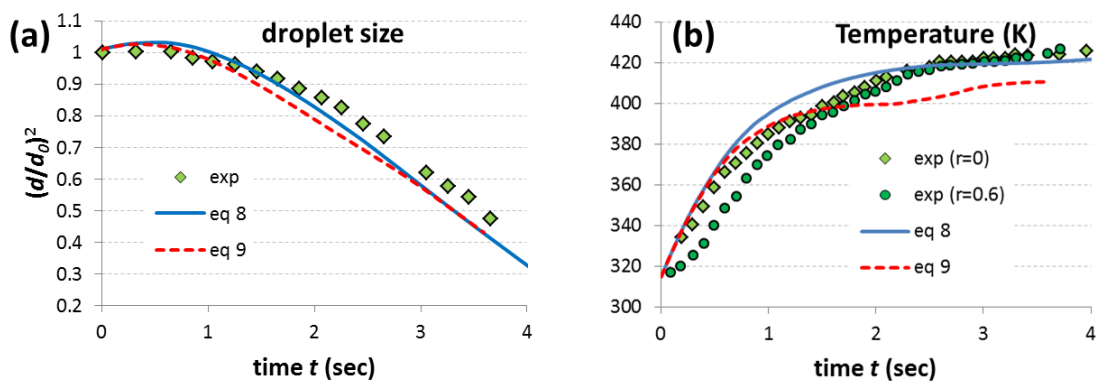
364

365 Fig. 8: Model predictions for the experimental data of Wong & Lin [60]. (a) temporal evolution
366 of droplet size and (b) mean droplet temperature.
367

368 The predicted flow, temperature and vapor concentration field for the experimental case of [60]
369 are shown in Fig. 9. The gravitational forces are quite strong and the droplet moves downwards
370 to the direction of gravity. Since the *Re* number of the flow is below 20, there is no recirculation
371 in the gas phase downwind the droplet and the temperature and vapor concentration fields have
372 a slightly different topology compared to the cases 1-3 presented in the previous section 4.1.
373 Furthermore, the thickness of the temperature and concentration boundary layers seem to be
374 higher compared to those of cases 1-3 and this ought to the fact that the boundary layer
375 thickness is proportional to $(RePr)^{-1/2}$ [70] as also to the thickening of the boundary layer due to
376 the intense evaporation rate [19].

377 Inside the droplet, the liquid circulation is quite disturbed forming two unsteady vortices which
378 tend to homogenize the temperature. This is in contradiction with the experimental observations
379 of Wong & Lin [60] as also with the numerical solution of Megaridis [30]. The inability to
380 capture this phenomenon in the current work is probably ought to the parasitic velocities
381 induced by the VOF methodology [71, 72], which originate from the imbalance between surface
382 tension and pressure gradient forces. The case examined has a low *Re* number and the parasitic
383 velocities become important while they are further magnified due to the high density ratio
384 between the liquid and the gas phase, which exceeds 2000 in this case. Nevertheless, the overall
385 behavior of droplet evaporation is not affected by the spurious currents and the experimental
386 data are correctly predicted. In an effort to reduce the magnitude of these velocities, several
387 options were examined, such as reducing the computational time-step down to a Courant
388 number of 0.1, increasing the smoothing iterations of VOF function and using different
389 discretization schemes for the VOF; however, none of these methods could improve the
390 predicted velocity field. The unphysical velocities could be potentially minimized by applying
391 the algorithm described in Francois et al. [72], but the pressure-velocity coupling in FLUENT is
392 hardcoded and cannot be modified as stated in [73]. The CSS surface tension scheme was also
393 examined, but the induced thermo-capillary flow along with the spurious velocities resulted in
394 high deformation of the droplet shape. Thus, the CSS simulations are not considered accurate
395 and they are not presented.

396
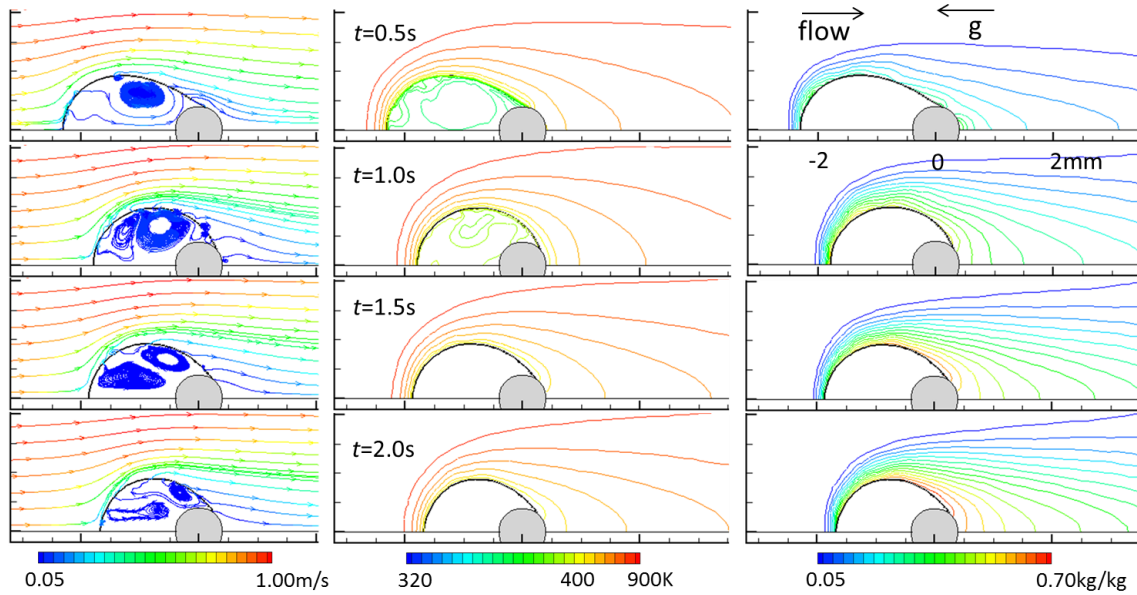
Fig. 9: Predicted flow field streamlines, temperature and vapor concentration field for the experimental case of Wong & Lin [60].

4.3 Evaporation at high temperature conditions. Experimental data of Nomura et al. [61]

Cases 5-8 of Table 1 correspond to the experimental data of Nomura et al. [61], who examined the evaporation of suspended n-heptane droplets for a wide range of ambient temperature and pressure conditions; these data have been widely used to validate 0-D and 1-D models (see [18, 39] among others). The experiments were conducted at microgravity conditions to prevent the natural convection and the vapor was flowing radially as stated in Nomura et al. [61]. The droplet diameters examined were in the range 0.6-0.8mm but the exact values were not reported. However, as the time axis of their plots was presented as t/d_0^2 this normalization results to the prediction of vaporization time independent on the selection of the droplet diameter. In the present work, a diameter of 0.7mm was selected as the mean among the experimental values. Regarding the initial droplet temperature, a value of 300K was used. Simulations of the cases of [61] were simplified by disabling the solution of the flow equations and accounting only for the transient and the diffusion terms in the conservation equations. This selection is justified by the fact that the velocities are quite low and the vapor flows radially [61]. Note that this is not equivalent to a 1-D model which assumes spherical symmetry, since a 2-D computation domain is used (Fig. 10) and the grid cells are not aligned with the liquid-gas interface (see inset figure in Fig. 10). More importantly, the gas phase temperature and concentration are also solved, so there is no need to estimate "film" gas properties near the interface, as also the Nusselt and

17

421 Sherwood numbers are not a-priori assumed, but become a part of the solution through the
422 predicted temperature and vapor concentration gradients. It has also to be noted that this
423 approach is not applicable in the experiments examined in the previous sections, since the gas
424 phase velocity plays a dominant role. The grid used is shown in Fig. 10 and it represents an
425 adiabatic box extended $25d_0$ far from the droplet. The box dimensions are large enough so that
426 the average gas temperature remains practically constant.

427
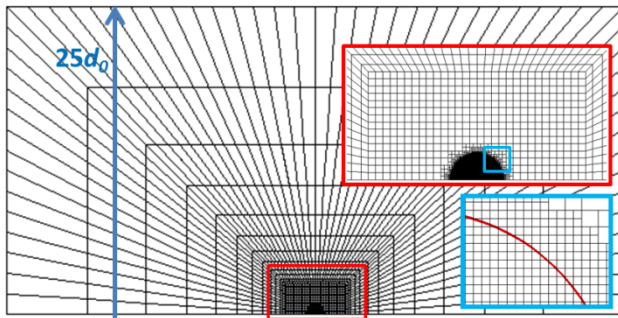
428

429 Fig. 10: Numerical grid used for the experimental data of Nomura et al. [61].
430

431 The model results for the dimensionless squared droplet diameter are shown in Fig. 11a for the
432 four different ambient temperatures examined. As it can be seen, the model results are
433 satisfactory for a wide range of ambient temperatures even above the critical one
434 ($T_{cr,C7}$=540.2K). The droplet evaporation rate is shown in Fig. 11b. The evaporation rate
435 increases at the initial stages of the evaporation due to droplet heat up and after reaching a
436 maximum it decreases due to the reduction of the droplet surface area. This behavior is observed
437 in all cases and it generally increases with increasing ambient temperature.

438
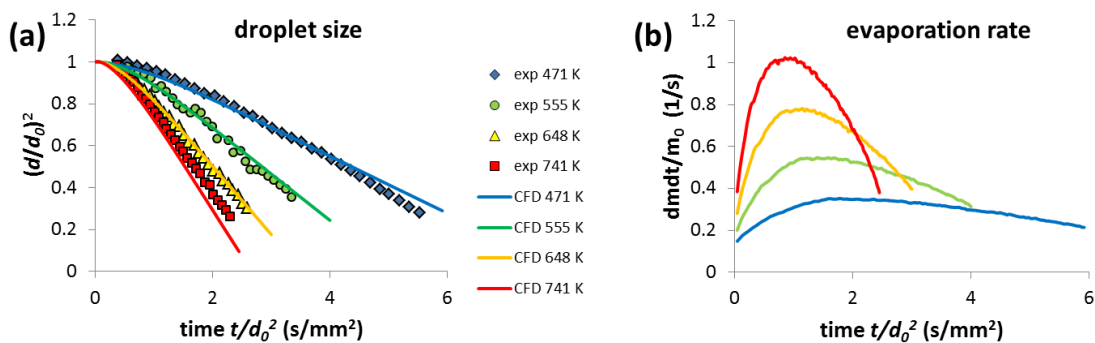
439

440 Fig. 11: Model predictions for the experimental data of Nomura et al. [61]. (a) temporal
441 evolution of droplet size and (b) evaporation rate.

18

442

443

5   CONCLUSIONS

The Navier-Stokes equations coupled with the conservation equations for energy and species concentration and the VOF methodology were used to study the evaporation of suspended single- and multi-component droplets. The local evaporation rate was estimated by using the Fick's diffusion law, which is independent of the interface shape and grid density. The model performance was assessed by comparing the results against experimental data for single- and bi-component fuel droplets under sub- and super-critical ambient temperature conditions. Prediction of the overall evaporation rate for a wide range of cases was satisfactory, while prediction of the droplet's temperature was within the accuracy of other published works. For the cases with *Re* of O(100) the recirculation zones at the gas and the liquid phase are correctly predicted and agree with the numerical solutions from other researchers. For the case with *Re* of O(10), the model could not capture the liquid phase internal recirculation zone since the parasitic velocities induced by the VOF methodology were large compared to the flow velocity. Overall, the numerical model can be considered as a reliable tool able to predict the lifetime and temporal evolution of droplet evaporation in a wide range of ambient temperature conditions for moderate and high Re numbers. In comparison to simplified (but also faster) 0-D and 1-D models, the present model gives insight into the spatial distribution of the flow variables and more importantly, it can be extended without any modification to predict the evaporation of deformed droplets and droplets undergoing breakup; see [74]. Nevertheless, with the today's computational resources, the present model cannot be used to simulate sprays comprised by a large number of droplets.

465

6   ACKNOWLEDGEMENTS

470

7 NOMENCLATURE

Symbol	Quantity	SI Unit
A	Surface area	m^2
B_M	Spalding number $B_M = \left(Y_{g,sat} - Y_{g,\infty}\right)/\left(1 - Y_{g,sat}\right)$	-
c_p	Specific heat capacity	$J/(kg\cdot K)$
d	Diameter	m
$\vec{d}$	Vector connecting adjacent cells	m
D	Mass diffusion coefficient	m^2/s
E	Specific internal energy	J/kg
F	Force	N
g	Gravity acceleration	m/s^2
h	Specific enthalpy	J/kg
$\mathbf{I}$	Unit tensor	-
$\vec{J}_{q,k}$	Species flux	kg/m^2s
k	Thermal conductivity coefficient	$W/(m\cdot K)$
L	Latent heat of vaporization	J/kg
$\dot{m}''$	Evaporation rate	kg/m^2s
$\dot{m}'''$	Evaporation source term	kg/m^3s
n	Normal coordinate to gas-liquid interface	-
Nph	Total number of phases	-
Nsp	Total number of liquid species	-
p	Pressure	N/m^2

Pr	Prandtl number	-
R	Radius	m
r	Coordinate in radial direction	m
Re	Reynolds number $Re = \rho_{g,\infty} d_0 u_\infty / \mu_{g,\infty}$	-
S	Source term	
T	Temperature	K
t	Time	s
u	Velocity	m/s
V	Volume	m^3
x,y,z	Coordinates	m
Y	Mass concentration	kg/kg

473

474 **Greek Symbols**

Symbol	Quantity	SI Unit
α	Liquid volume fraction	-
κ	Curvature	m^{-1}
μ	Viscosity	kg/(m·s)
ρ	Density	kg/m^3
σ	Surface tension coefficient	N/m

475

476 **Subscripts**

Symbol	Quantity
0	Initial
∞	Conditions far from the droplet

21

cell	Cell
cr	Critical
d	Droplet
evap	Evaporation
exp	Experimental
g	Gas phase
k	k^{th} species of the mixture
l	Liquid phase
m	Mixture
mean	Mean
q	of phase q
sat	Saturated
surf	Surface interface
vap	Vapor

477

478 **abbreviations**

C10	n-decane
C7	n-heptane
CSF	Continuum Surface Force
CSS	Continuum Surface Stress
ECM	Effective Conductivity Model
FCM	Finite Conductivity Model
FDM	Finite Diffusivity Model
ICM	Infinite Conductivity Model

IDM   Infinite Diffusivity Model

VOF   Volume Of Fluid

479

480

8   REFERENCES

482

[1] Clift R., Grace J.R., Weber M.E., Bubbles, drops and particles, Academic Press, New York, 1978.

[2] Sirignano W.A., Fluid Dynamics and Transport of Droplets and Sprays, Cambridge University Press, 1999.

[3] Bird R.B., Stewart W.E., Lightfoot E.N., Transport Phenomena, 2nd ed., Wiley, New York, 2002.

[4] Asano K., Mass Transfer – from Fundamentals to Modern Industrial Applications, Wiley VCH Verlag GmbH & Co. KGaA, Weinheim, Germany, 2006.

[5] Givler S.D., Abraham J., Supercritical droplet vaporization and combustion studies, Progress in Energy and Combustion Science, 22 (1996) 1-28.

[6] Bellan J., Supercritical (and subcritical) fluid behavior and modeling: drops, streams, shear and mixing layers, jets and sprays, Progress in Energy and Combustion Science, 26 (2000) 329-366.

[7] Sazhin S.S., Advanced models of fuel droplet heating and evaporation, Progress in Energy and Combustion Science, 32 (2006) 162-214.

[8] Erbil H.Y., Evaporation of pure liquid sessile and spherical suspended drops: A review, Advances in Colloid and Interface Science, 170 (2012) 67-86.

[9] Godsave G.A.E., Burning of Fuel Droplets in: 4th International Symposium on combustion, The Combustion Institute, Baltimore, 1953, pp. 818-830.

[10] Spalding D.B., The combustion of liquid fuels, in: 4th International Symposium on combustion, The Combustion Institute, Baltimore, 1953, pp. 847-864.

504   [11] Law C.K., Unsteady droplet combustion with droplet heating, Combustion and Flame, 26
505   (1976) 17-22.

506   [12] Law C.K., Sirignano W.A., Unsteady droplet combustion with droplet heating--II:
507   Conduction limit, Combustion and Flame, 28 (1977) 175-186.

508   [13] Abramzon B., Sirignano W.A., Droplet vaporization model for spray combustion
509   calculations, International Journal of Heat and Mass Transfer, 32 (1989) 1605-1618.

510   [14] Dombrovsky L.A., Sazhin S.S., A parabolic temperature profile model for heating of
511   droplets, Journal of Heat Transfer, 125 (2003) 535-537.

512   [15] Yao G.F., Abdel-Khalik S.I., Ghiaasiaan S.M., An Investigation of Simple Evaporation
513   Models Used in Spray Simulations, Journal of Heat Transfer, 125 (2003) 179-182.

514   [16] Miller R.S., Harstad K., Bellan J., Evaluation of equilibrium and non-equilibrium
515   evaporation models for many-droplet gas-liquid flow simulations, International Journal of
516   Multiphase Flow, 24 (1998) 1025-1055.

517   [17] Kolaitis D.I., Founti M.A., A comparative study of numerical models for Eulerian-
518   Lagrangian simulations of turbulent evaporating sprays, International Journal of Heat and Fluid
519   Flow, 27 (2006) 424-435.

520   [18] Sazhin S.S., Kristyadi T., Abdelghaffar W.A., Heikal M.R., Models for fuel droplet heating
521   and evaporation: Comparative analysis, Fuel, 85 (2006) 1613-1630.

522   [19] Zhifu Z., Guoxiang W., Bin C., Liejin G., Yueshe W., Evaluation of Evaporation Models
523   for Single Moving Droplet with a High Evaporation Rate, Powder Technology, 240 (2013) 95-
524   102.

525   [20] Law C.K., Multicomponent droplet combustion with rapid internal mixing, Combustion
526   and Flame, 26 (1976) 219-233.

527   [21] Renksizbulut M., Bussmann M., Li X., Droplet vaporization model for spray calculations,
528   Particle & Particle Systems Characterization, 9 (1992) 59-65.

529   [22] Varanasi K.K., Clack H.L., Miller R.S., On preferential diffusion of binary component
530   liquid droplets evaporating in a two-phase mixing layer, International Journal of Multiphase
531   Flow, 30 (2004) 1235-1257.

532   [23] Law C.K., Internal boiling and superheating in vaporizing multicomponent droplets,

533   AIChE Journal, 24 (1978) 626-632.

534   [24] Kneer R., Schneider M., Noll B., Wittig S., Diffusion controlled evaporation of a

535   multicomponent droplet: theoretical studies on the importance of variable liquid properties,

536   International Journal of Heat and Mass Transfer, 36 (1993) 2403-2415.

537   [25] Torres D.J., O'Rourke P.J., Amsden A.A., Efficient multicomponent fuel algorithm,

538   Combustion Theory and Modelling, 7 (2003) 67-86.

539   [26] Brenn G., Concentration fields in evaporating droplets, International Journal of Heat and

540   Mass Transfer, 48 (2005) 395-402.

541   [27] Renksizbulut M., Haywood R.J., Transient droplet evaporation with variable properties and

542   internal circulation at intermediate Reynolds numbers, International Journal of Multiphase

543   Flow, 14 (1988) 189-202.

544   [28] Haywood R.J., Nafziger R., Renksizbulut M., Detailed examination of gas and liquid phase

545   transient processes in convective droplet evaporation, Journal of Heat Transfer, 111 (1989) 495-

546   502.

547   [29] Chiang C.H., Raju M.S., Sirignano W.A., Numerical analysis of convecting, vaporizing

548   fuel droplet with variable properties, International Journal of Heat and Mass Transfer, 35 (1992)

549   1307-1324.

550   [30] Megaridis C.M., Comparison between experimental measurements and numerical

551   predictions of internal temperature distributions of a droplet vaporizing under high-temperature

552   convective conditions, Combustion and Flame, 93 (1993) 287-302.

553   [31] Shih A.T., Megaridis C.M., Suspended droplet evaporation modeling in a laminar

554   convective environment, Combustion and Flame, 102 (1995) 256-270.

555   [32] Shih A.T., Megaridis C.M., Thermocapillary flow effects on convective droplet

556   evaporation, International Journal of Heat and Mass Transfer, 39 (1996) 247-257.

557   [33] Abou Al-Sood M.M., Birouk M., A numerical study of the effect of turbulence on mass

558   transfer from a single fuel droplet evaporating in a hot convective flow, International Journal of

559   Thermal Sciences, 46 (2007) 779-789.

560   [34] Raghuram S., Raghavan V., Pope D.N., Gogos G., Two-phase modeling of evaporation

561   characteristics of blended methanol–ethanol droplets, International Journal of Multiphase Flow,

562   52 (2013) 46-59.

563   [35] Megaridis C.M., Sirignano W.A., Numerical modeling of a vaporizing multicomponent

564   droplet, Symposium (International) on Combustion, 23 (1990) 1413-1421.

565   [36] Megaridis C.M., Sirignano W.A., Multicomponent droplet vaporization in a laminar

566   convective environment, Combustion science and technology, 87 (1992) 27-44.

567   [37] Megaridis C.M., Liquid-Phase Variable Property Effects in Multicomponent Droplet

568   Convective Evaporation, Combustion Science and Technology, 92 (1993) 291 - 311.

569   [38] Renksizbulut M., Bussmann M., Multicomponent droplet evaporation at intermediate

570   Reynolds numbers, International Journal of Heat and Mass Transfer, 36 (1993) 2827-2835.

571   [39] Zhang H., Evaporation of a suspended droplet in forced convective high-pressure

572   environments, Combustion Science and Technology, 175 (2003) 2237-2268.

573   [40] Haywood R.J., Renksizbulut M., Raithby G.D., Transient deformation and evaporation of

574   droplets at intermediate Reynolds numbers, International Journal of Heat and Mass Transfer, 37

575   (1994) 1401-1409.

576   [41] Schlottke J., Weigand B., Direct numerical simulation of evaporating droplets, Journal of

577   Computational Physics, 227 (2008) 5215-5237.

578   [42] Strotos G., Gavaises M., Theodorakakos A., Bergeles G., Numerical investigation of the

579   evaporation of two-component droplets, Fuel, 90 (2011) 1492-1507.

580   [43] Banerjee R., Numerical investigation of evaporation of a single ethanol/iso-octane droplet,

581   Fuel, 107 (2013) 724-739.

582   [44] Ghata N., Shaw B.D., Computational modeling of the effects of support fibers on

583   evaporation of fiber-supported droplets in reduced gravity, International Journal of Heat and

584   Mass Transfer, 77 (2014) 22-36.

585   [45] Malgarinos I., Nikolopoulos N., Marengo M., Antonini C., Gavaises M., VOF simulations

586   of the contact angle dynamics during the drop spreading: Standard models and a new wetting

587   force model, Advances in Colloid and Interface Science, 212 (2014) 1-20.

588   [46] Malgarinos I., Nikolopoulos N., Gavaises M., Coupling a local adaptive grid refinement
589   technique with an interface sharpening scheme for the simulation of two-phase flow and free-
590   surface flows using VOF methodology, Journal of Computational Physics, 300 (2015) 732-753.

591   [47] Strotos G., Malgarinos I., Nikolopoulos N., Papadopoulos K., Theodorakakos A., Gavaises
592   M., Performance of VOF methodology in predicting the deformation and breakup of
593   impulsively accelerated droplets in: 13th ICLASS, Tainan, Taiwan, 2015.

594   [48] Hirt C.W., Nichols B.D., Volume of Fluid (Vof) Method for the Dynamics of Free
595   Boundaries, Journal of Computational Physics, 39 (1981) 201-225.

596   [49] Brackbill J.U., Kothe D.B., Zemach C., A continuum method for modeling surface tension,
597   Journal of Computational Physics, 100 (1992) 335-354.

598   [50] Lafaurie B., Nardone C., Scardovelli R., Zaleski S., Zanetti G., Modelling Merging and
599   Fragmentation in Multiphase Flows with SURFER, Journal of Computational Physics, 113
600   (1994) 134-147.

601   [51] Perry R.H., Green D.W., Perry's Chemical Engineers' Handbook, 7th ed., McGraw-Hill,
602   1997.

603   [52] Poling B.E., Prausnitz J.M., O'Connell J.P., Properties of Gases and Liquids (5th Edition),
604   in, McGraw-Hill, 2001.

605   [53] Youngs D.L., Time-Dependent Multi-Material Flow with Large Fluid Distortion, in:
606   Morton K.W., Baines M.J. (Eds.) Numerical Methods for Fluid Dynamics,, Academic Press,
607   New York, 1982.

608   [54] Barth T., Jespersen D., The design and application of upwind schemes on unstructured
609   meshes, in: 27th Aerospace Sciences Meeting, American Institute of Aeronautics and
610   Astronautics, 1989.

611   [55] ANSYS®FLUENT, Release 14.5, Theory Guide, in, 2012.

612   [56] Issa R.I., Solution of implicitly discretised fluid flow equations by operator-splitting,
613   Journal of Computational Physics, 62 (1986) 40-65.

614   [57] Hu H., Larson R.G., Evaporation of a sessile droplet on a substrate, Journal of Physical
615   Chemistry B, 106 (2002) 1334-1344.

616   [58] Mollaret R., Sefiane K., Christy J.R.E., Veyret D., Experimental and numerical

617   investigation of the evaporation into air of a drop on a heated surface, Chemical Engineering

618   Research & Design, 82 (2004) 471-480.

619   [59] Daïf A., Bouaziz M., Chesneau X., Ali Cherif A., Comparison of multicomponent fuel

620   droplet vaporization experiments in forced convection with the Sirignano model, Experimental

621   Thermal and Fluid Science, 18 (1999) 282-290.

622   [60] Wong S.C., Lin A.C., Internal temperature distributions of droplets vaporizing in high-

623   temperature convective flows, Journal of Fluid Mechanics, 237 (1992) 671-687.

624   [61] Nomura H., Ujiie Y., Rath H.J., Sato J.I., Kono M., Experimental study on high-pressure

625   droplet evaporation using microgravity conditions, in: Symposium (International) on

626   Combustion, 1996, pp. 1267-1273.

627   [62] Theodorakakos A., Bergeles G., Simulation of sharp gas–liquid interface using VOF

628   method and adaptive grid local refinement around the interface, International Journal for

629   Numerical Methods in Fluids, 45 (2004) 421-439.

630   [63] Zeng Y., Lee C.F., A model for multicomponent spray vaporization in a high-pressure and

631   high-temperature environment, Journal of Engineering for Gas Turbines and Power, 124 (2002)

632   717-724.

633   [64] Ozturk A., Cetegen B.M., Modeling of plasma assisted formation of precipitates in

634   zirconium containing liquid precursor droplets, Materials Science and Engineering A, 384

635   (2004) 331-351.

636   [65] Strotos G., Gavaises M., Theodorakakos A., Bergeles G., Evaporation of a suspended

637   multicomponent droplet under convective conditions, in: ICHMT, Marrakech, Morocco, 2008.

638   [66] Taneda S., Experimental Investigation of the Wake behind a Sphere at Low Reynolds

639   Numbers, J. Phys. Soc. Japan, 11 (1956) 1104-1108.

640   [67] Amani E., Nobari M.R.H., A calibrated evaporation model for the numerical study of

641   evaporation delay in liquid fuel sprays, International Journal of Heat and Mass Transfer, 56

642   (2013) 45-58.

643   [68] Tonini S., Cossali G.E., A novel vaporisation model for a single-component drop in high

644   temperature air streams, International Journal of Thermal Sciences, 75 (2014) 194-203.

645   [69] Abramzon B., Sazhin S., Convective vaporization of a fuel droplet with thermal radiation

646   absorption, Fuel, 85 (2006) 32-46.

647   [70] Feng Z.-G., Michaelides E.E., Heat and mass transfer coefficients of viscous spheres,

648   International journal of heat and mass transfer, 44 (2001) 4445-4454.

649   [71] Harvie D.J.E., Davidson M.R., Rudman M., An analysis of parasitic current generation in

650   Volume of Fluid simulations, Applied Mathematical Modelling, 30 (2006) 1056-1066.

651   [72] Francois M.M., Cummins S.J., Dendy E.D., Kothe D.B., Sicilian J.M., Williams M.W., A

652   balanced-force algorithm for continuous and sharp interfacial surface tension models within a

653   volume tracking framework, Journal of Computational Physics, 213 (2006) 141-173.

654   [73] Bohacek J., Surface Tension Model for High Viscosity Ratios Implemented in VOF Model,

655   in: ILASS - Europe, Brno, Czech Republic, 2010.

656   [74] Strotos G., Malgarinos I., Nikolopoulos N., Gavaises M., Numerical investigation of

657   aerodynamic droplet breakup in a high temperature gas environment, Fuel, 181 (2016) 450-462.

658

659